Demonstration and uncertainty analysis of synchronised scanning lidar measurements of 2D velocity fields in a boundary-layer wind tunnel

Marijn F. van Dooren[1], Filippo Campagnolo[2], Mikael Sjöholm[3], Nikolas Angelou[3], Torben Mikkelsen[3], and Martin Kühn[1]

[1]ForWind, University of Oldenburg, Institute of Physics, Oldenburg, Germany
[2]Wind Energy Institute, Technical University of Munich, Garching, Germany
[3]Dept. of Wind Energy, Technical University of Denmark, Roskilde, Denmark

Correspondence to: Marijn F. van Dooren (marijn.vandooren@uni-oldenburg.de)

Abstract. This paper combines the currently relevant research methodologies of scaled wind turbine model experiments in wind tunnels with remote-sensing short-range WindScanner lidar measurement technology. The wind tunnel of the Politecnico di Milano was equipped with three wind turbine models and two short-range WindScanner lidars to demonstrate the benefits of synchronised scanning lidars in such experimental surroundings for the first time. The dual-lidar system can provide fully
5 synchronised trajectory scans with sampling time scales ranging from seconds to minutes. First, staring mode measurements were compared to hot-wire probe measurements commonly used in wind tunnels. This yielded goodness of fit coefficients of 0.969 and 0.902 for the 1 Hz averaged u- and v-components of the wind speed, respectively, validating the 2D measurement capability of the lidar scanners. Subsequently, the measurement of wake profiles on a line as well as wake area scans were executed to illustrate the applicability of lidar scanning to measuring small scale wind flow effects. An extensive uncertainty
10 analysis was executed to assess the accuracy of the method. The downsides of lidar with respect to the hot-wire probes are the larger measurement probe volume and the loss of some measurements due to moving blades. In contrast, the benefits are the high flexibility in conducting both point measurements and area scanning, and the fact that remote sensing techniques do not disturb the flow while measuring. The research campaign revealed a high potential for using short-range synchronised scanning lidars to accurately measure small scale flow structures in a wind tunnel, and increased the knowledge about the corresponding
15 uncertainties.

1 Introduction

During the past few years, several research groups have focused attention on wind tunnel experiments with the innovative idea of supporting research not only related to the validation of purely aerodynamic models, but mainly to support numerical activities on control and aero-servo-elasticity (Bottasso et al., 2014) as well as understanding the interaction of wind turbines
20 with turbulent flow (Rockel et al., 2014). In fact, testing of wind turbines in full-scale in the atmospheric boundary-layer imposes several constraints, such as the difficulty in having an accurate knowledge and repeatability of the environmental

conditions, higher costs, and especially for public researchers, the difficulty to have access to industrial wind turbines as a research platform. In the same period, academic and industrial researchers have developed new scanning wind lidars able to map full three-dimensional vector wind and turbulence fields in 3D space (Mikkelsen, 2012; Wagner et al., 2015; Simley et al., 2016). Even for complex flows, such as the flow around wind turbines, the lidars can be applied without disturbing the flow

5   itself. The present work reports on the testing activity conducted recently by a joint team of research groups, where two short-range WindScanners have been tested in a boundary-layer test section of a wind tunnel for the first time, in order to map the flow of the free chamber as well as to accurately measure the wakes of scaled wind turbine models. This measurement campaign was executed in the scope of the CompactWind project, which has the purpose of investigating the effect of different wind farm control concepts and yaw configurations of the individual turbines on the wind farm energy output, the wake structures

10   and wind turbine loads (Campagnolo et al., 2016). The following is based on material published before at the TORQUE 2016 conference (van Dooren et al., 2016a).

2   Methodology

2.1   The wind tunnel facility

In January 2016, three generically scaled wind turbine models (see Fig. 1), specifically designed by the Wind Energy Institute

15   (WEI) at the Technical University of Munich (TUM) for wind farm control research applications, as well as two short-range WindScanners (see Fig. 2) developed by the Department of Wind Energy of the Technical University of Denmark (DTU) were installed in the wind tunnel of the Politecnico di Milano (PoliMi).
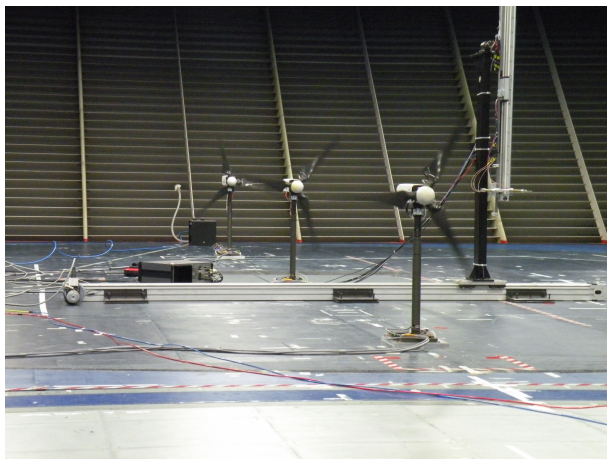
Figure 1. Model wind turbines in operation in the wind tunnel.   **Figure 2.** One of the two WindScanner lidars inside the wind tunnel.
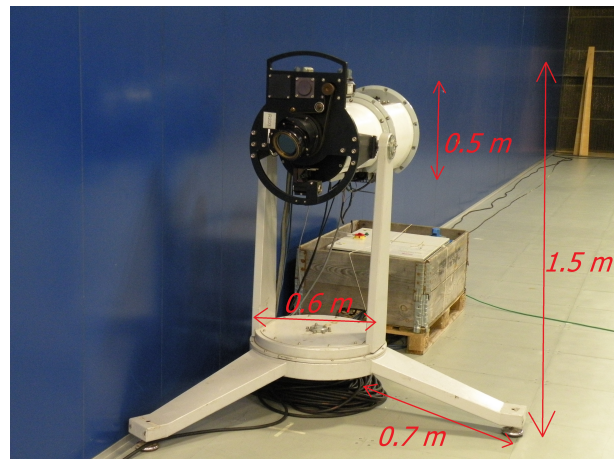
The PoliMi wind tunnel has a closed-return configuration facility arranged in a vertical layout with two test sections. The

20   boundary-layer test section, sketched in Fig. 3, is located at the upper level in the return duct and has a cross-sectional area of 13.84 m by 3.84 m and a length of 36 m, illustrated by the blue outer boundaries in Fig. 3. The three wind turbines were

mounted on a turn table which allows for rotating the entire turbine array setup, as to create a lateral offset between the wind turbines. When the turn table is in its 'home position', the turbines line up in x-direction with a distance of $4D$ between them. The WindScanners are indicated with red rectangles and their commanded synchronised scan pattern for scanning the wind turbine wakes is plotted in grey. Atmospheric boundary-layer conditions can be simulated by the use of turbulence generators,

5   i.e. spires, placed at the chamber inlet at the left boundary. For more information about the wind tunnel, please refer to Zasso et al. (2005).
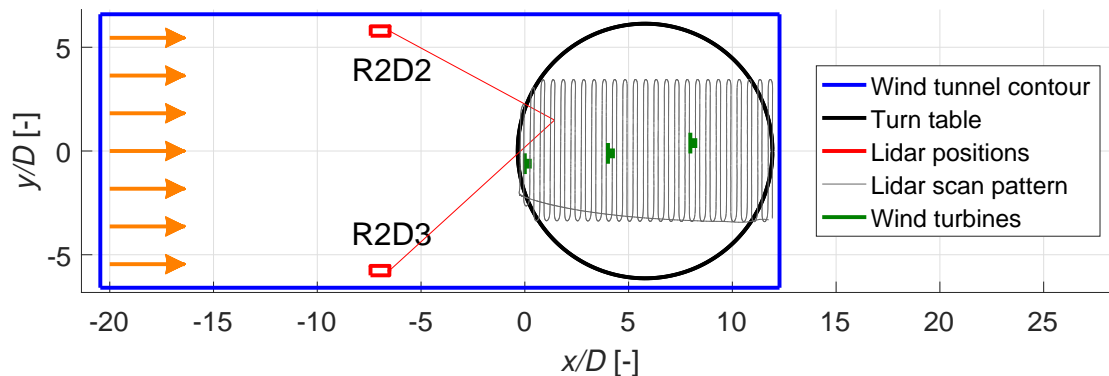
Figure 3. Configuration of the wind tunnel of the Politecnico di Milano with the two scanning lidars and the three model wind turbines installed on the turn table. The axes are normalised with respect to the wind turbine diameter of $D = 1.1$ m.

2.2   The G1 wind turbine models

The three scaled *G1* wind turbine models (Bottasso et al., 2014) have a rotor diameter D of 1.1 m, a hub height of 0.825 m and a rated rotor speed equal to 850 rpm. They were designed to provide a realistic energy conversion process, which means

10   reasonable aerodynamic loads and damping when compared to those of full-scale wind turbines, as well as wakes with a realistic geometry, velocity deficit and turbulence intensity. Moreover, systems have been integrated to enable individual blade pitch, torque and yaw control, while a sufficient onboard sensor equipment of the machine, providing measurements of rotor azimuth, main shaft loads, rotor speed and tower base loads, enables the testing of both wind turbine and wind farm control strategies.

15   Each *G1* model is equipped with three blades whose pitch angles can be varied by means of brushed motors housed in the hollow roots of the blades and commanded by dedicated electronic control boards housed in the hub spinner. Electrical signals from and to the pitch control boards are transmitted by a through-bore 12-channels slip ring located within the rectangular carrying box holding the main shaft. A torque sensor allows for the measurement of the torque provided by a brushless motor located in the rear part of the nacelle, which is operated as a generator by using a servo-controller. An optical encoder, located

20   between the slip ring and the rear shaft bearing, allows for the measurement of the rotor azimuth. The tower is softened at

its base by machining four small bridges, on which strain gauges are glued so as to measure fore-aft and side-side bending moments. Aerodynamic covers of the nacelle and hub ensure a satisfactory quality of the flow in the central rotor area.

Each *G1* model is controlled by an *M1 Bachmann* hardware real-time module. Similarly to what is done on real wind turbines, collective or individual pitch-torque control laws are implemented on and real-time executed by the control hardware.
5   Sensor readings are used online to properly compute the desired pitch and torque demands, which are in turn sent to the actuator control boards via analog or digital communication.

2.3   The short-range WindScanner lidars

The two short-range WindScanners R2D2 and R2D3, installed near the section walls upwind of the turbine models (see Fig. 3), are continuous-wave, coherent Doppler lidars that can provide averaged wind speeds at rates up to 390 Hz. The measurement
10   range is defined by the focus distance which is motor controlled between about 9 m and 150 m. The longitudinal line-of-sight sampling volumes can become very small at short ranges, e.g. about 13 cm probe length at a 10 m focus distance, thus the WindScanners were placed as close as possible to the measurement area of interest, within the reachable focus distances. The laser beam can be freely steered within a cone with a full opening angle of 120° by the use of two prisms. The two prism motors and focus motor that each system comprises are synchronously operated by a common central motion controller that
15   steers all the six motors such that the two focused laser beams can synchronously follow a common scanning trajectory. The laser beam focus point of each WindScanner was pre-calibrated at DTU and the location and orientation of the WindScanners relative to the wind tunnel and the wind turbines were achieved by inclination measurements and a Leica total station in combination with well localised rotating hard targets that give a distinct Doppler lidar return signature. Additional verification of the measurement locations was done by the use of infrared sensitive equipment.

20   Each lidar measures a projected line-of-sight component of the three-dimensional wind velocity vector. From two temporally and spatially synchronised line-of-sight measurements v_{LOS}, the u- and v-components of the wind speed, defined along and lateral to the main wind direction respectively, can be calculated by solving the linear equation system in Eq. (1):

$$\begin{bmatrix} \cos(\chi_1)\cos(\delta_1) & \sin(\chi_1)\cos(\delta_1) \\ \cos(\chi_2)\cos(\delta_2) & \sin(\chi_2)\cos(\delta_2) \end{bmatrix} \begin{bmatrix} u \\ v \end{bmatrix} = \begin{bmatrix} v_{LOS_1} \\ v_{LOS_2} \end{bmatrix} \tag{1}$$

In this linear system, the influence of the vertical wind component w is neglected. A third lidar would be needed to evaluate
25   this additional component. The horizontal and vertical scanning angles of a lidar system are the azimuth χ and elevation δ angles, respectively. Because the lidar scan heads are located slightly higher than the turbine hub height, small negative elevation angles $\delta < 3°$ had to be used. It is assumed that this causes an insignificant contamination of the result by the w-component.

As mentioned before, the lidars acquire each measurement based on the aerosols present in a certain probe volume, which is
30   illustrated qualitatively in Fig. 4. The value of the probe length is commonly defined as twice the Half Width Half Maximum Γ, which is the distance at either side of the focus point at which the backscatter signal power is reduced to half of its maximum

power. The power spectrum of the backscattered signal can be expressed with a Lorentzian probability distribution along the beam line-of-sight direction, multiplied by the line-of-sight wind speed component at the corresponding coordinates. The probe length increases quadratically with the focus distance, which is expressed in Eq. (2) and plotted in Fig. 5.
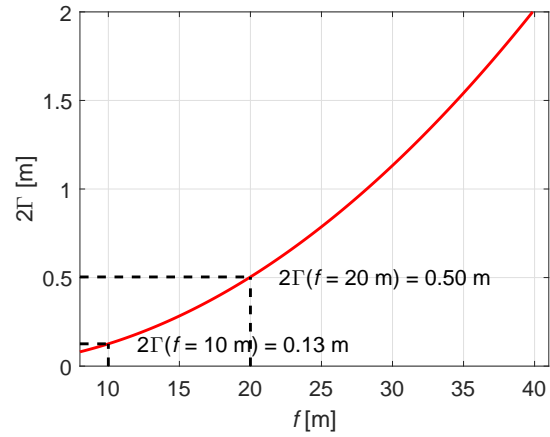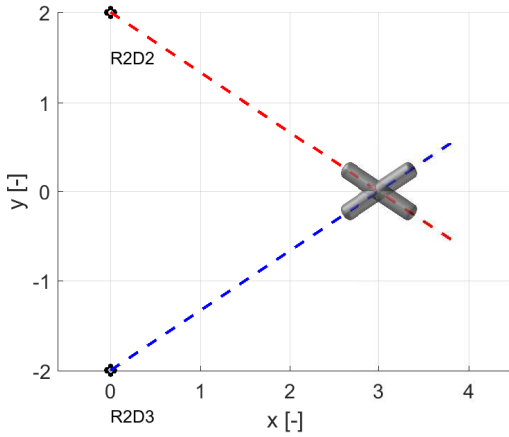
Figure 4. Sketch of the probe volumes of both lidars (not to scale). **Figure 5.** Relationship between focus distance and the probe length.

$$\Gamma = \frac{\lambda f^2}{\pi a^2} \tag{2}$$

In Eq. (2), Γ is the Half Width Half Maximum, λ is the lidar laser wavelength, f is the focus distance and a is the laser beam width at the aperture.

2.4 The hot-wire probe

A tri-axial Dantec 55R91 hot-wire probe (see Fig. 6) was mounted on an automatic traversing system (see Fig. 7) and provided 2500 Hz measurements of the three-dimensional wind speed vector in the wind tunnel. The three wires of the hot-wire probe form an orthogonal system with respect to each other and are also positioned orthogonally to the prongs of the probe for increased accuracy. The effective sensor length of each of the wires is 1.25 mm. The hot-wire anemometer had been calibrated in a dedicated open circuit wind tunnel at PoliMi before.
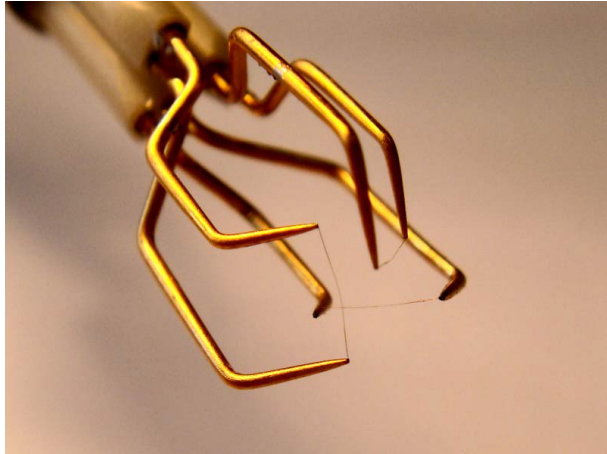
Figure 6. The tri-axial Dantec 55R91 hot-wire probe.
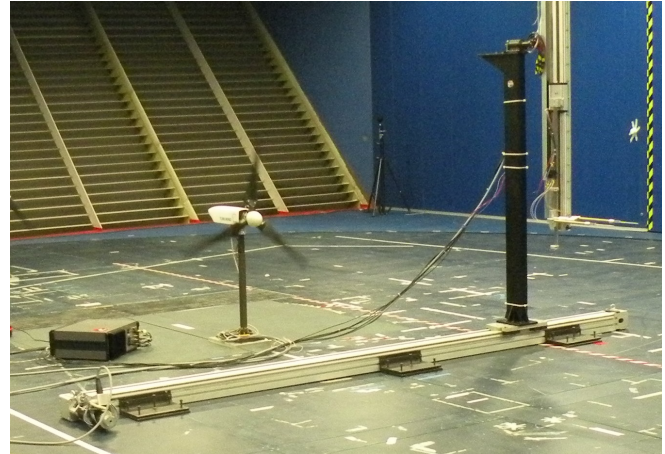
Figure 7. The traversing system for the hot-wire probes.

2.5 Measurement examples

The measurement campaign covered several scenarios. In this paper, only relevant examples from the three main types of measurements are presented to illustrate the capabilities:

1. *Comparison between lidar and hot-wire probe measurements*: The lidar beams were focused as closely to the hot-wire as practically possible, i.e. without influencing the hot-wire probe due to heating by the laser beams on the one hand, or blocking the view of the lidars with the hot-wire probe and the traversing system on the other. The focus offset was chosen to be 2 cm. A series of different points in the wind tunnel were measured by both anemometers for a duration of 2 minutes each. In this case, the data of a single point at $x = 2.23$ m, $y = 0.88$ m, $z = 0.83$ m is considered for analysis. The wind turbines were idling at approximately 80 rpm and this is assumed to have a negligible effect on the flow at the considered measurement point.

2. *Measurement of wake profiles along a horizontal line*: The lidars performed measurements back and forth along cross-wind lines at several distances downstream of the first wind turbine at hub height and spanning $\pm 3.5D$ around the wake centre. The complete line was covered every 1 s with equally sampled measurements. In the case presented, a wake profile at a $3D$ downstream distance of the first wind turbine is analysed. All turbines are operating under rated conditions. The first and second turbines have yaw offsets of $20°$ and $10°$, respectively.

3. *Measurement of horizontal wake area scans*: The full area containing the three wakes of the model turbines were mapped by the lidars by iterating through the scanning pattern already indicated in Fig. 3. The scans cover an area of 7 by 13 m every 18.5 s. Multiple scans were averaged to resolve the mean wake features. All turbines are operating under rated conditions and have no yaw offset.

The inflow conditions were regulated to be constant. The free-stream wind speed and the turbulence intensity, both at hub height, were $u_0 = 5.67$ m s^{-1} and $TI = 5\%$, respectively. The vertical wind profile corresponded to a power law profile with shear exponent $\alpha = 0.08$.

3 Results

3.1 Comparison between lidar and hot-wire probe measurements

The first step of the lidar campaign in the wind tunnel was to establish a quantitative measure of the accuracy of the lidars with respect to the commonly applied devices in such an environment, i.e. hot-wire anemometers. Here, the established hot-wire probe served as a validation for the lidar measurements. In order to compare the devices directly with each other, the hot-wire probe data recorded at 2500 Hz has been averaged to match the lidar measurement frequency of 390 Hz. Subsequently, the data of both devices was averaged to 1 Hz and compared again.

In Table 1 the mean (μ) and standard deviation (σ) of the u-, v-, and w-components from a single 2-minute point measurement time series of both systems can be seen. The u-, v- and w-components of the hot-wire are directly measured and the u- and v-components of the lidars are derived from the line-of-sight measurements by applying Eq. (1). The w-component cannot be evaluated from the lidar measurements in this case and is therefore neglected. The u-, v- and w-components are expressed in the x-, y- and z-direction of the lidar reference frame, respectively, which is indicated in the wind tunnel configuration sketch (see Fig. 3). The hot-wire probe measurements originally obtained in a different coordinate system were transformed into the lidar frame of reference. Time synchronisation between the devices was taken care of by a cross-correlation optimisation.

Table 1. Statistics of the wind speed components measured at a point over a 2-minute time frame with the hot-wire probe and the lidars.

	Hot-wire			Lidar	
	u	v	w	u	v
μ	5.67	-0.04	0.08	5.65	-0.03
σ	0.31	0.28	0.26	0.28	0.27

Correlation plots of both the u- and v-components are shown in Figs. 8 and 9, respectively. Although the regression line does not perfectly resemble $x = y$ and some scattering is visible, the measurements yielded very reasonable - especially for the considered sampling rate - goodness of fit coefficients of $R^2 = 0.777$ for the u-component and $R^2 = 0.633$ for the v-component. Possible reasons for the remaining scatter in the plot are:

– The probe volumes of the anemometers differ and they are not measuring in the exact same point or volume, so that different fluctuations are seen by the different devices.

– The contribution of the w-component on the measured v_{LOS} is neglected.

- There might be a small bias in the transformation between the different coordinate systems of the lidars and the hot-wire probe, causing a cross-contamination in the calculation of both wind speed components u and v.
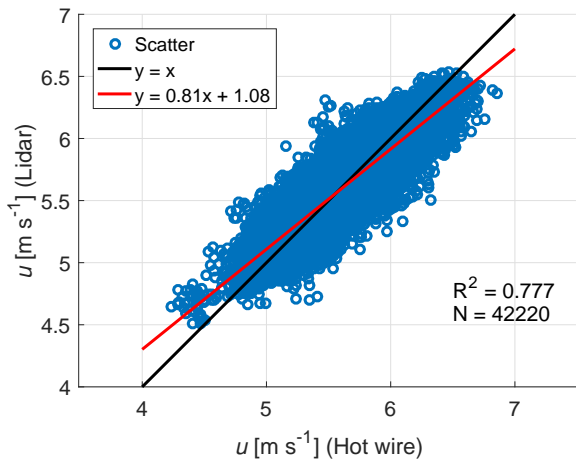
Figure 8. Correlation of the 390 Hz u-component.
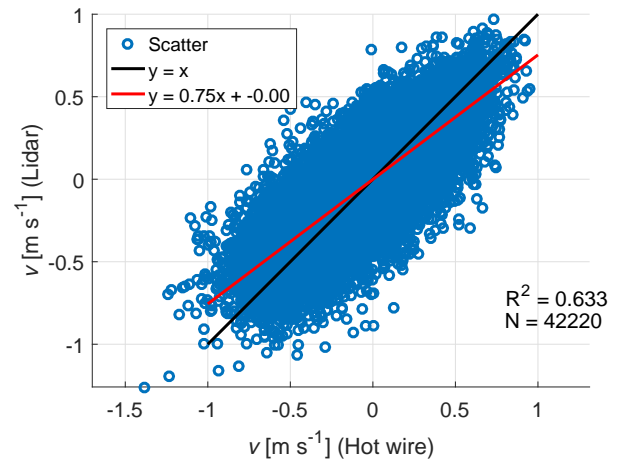
Figure 9. Correlation of the 390 Hz v-component.

The time series were subsequently further averaged to 1 Hz data. Showing both data sets in the same plot, Figs. 10 and 11

5   display the u- and v-components, respectively. On this time scale, it can be concluded visually that the measurements correlate very well.
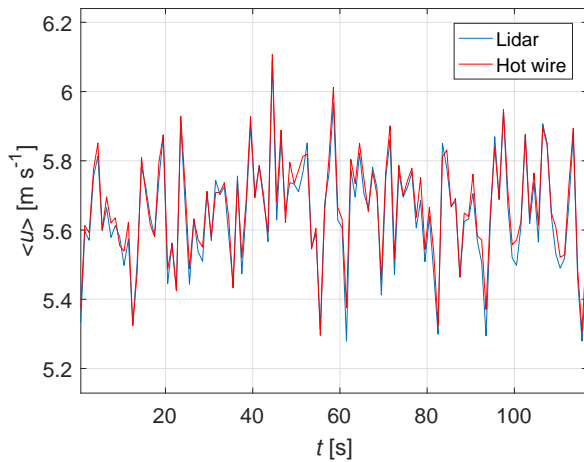
Figure 10. Visual comparison of the 1 Hz averaged u-component.
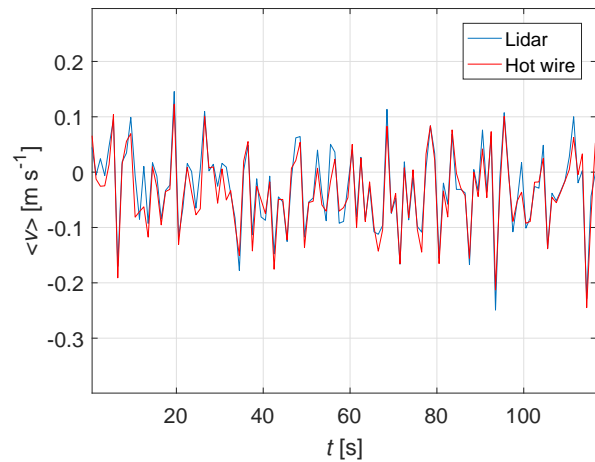
Figure 11. Visual comparison of the 1 Hz averaged v-component.

The 1 Hz averaged u- and v-components in Figs. 10 and 11 were correlated with each other, as shown by Figs. 12 and 13.
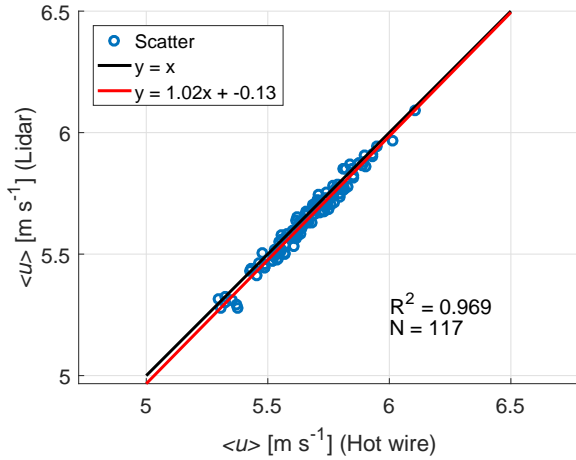
Figure 12. Correlation of the 1 Hz averaged u-component.
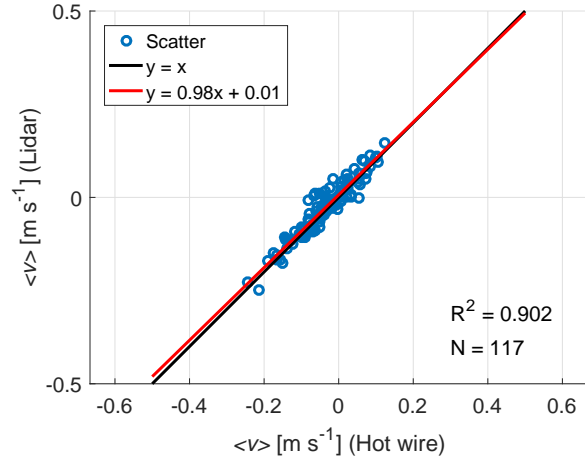
Figure 13. Correlation of the 1 Hz averaged v-component.

The mentioned effects that caused the scatter in the correlated 390 Hz data of Figs. 8 and 9 do not play a large role anymore after the data has been averaged to 1 Hz time series, since most of the very small scale fluctuations are omitted here. Correlating the 1 Hz averaged data now provided the goodness of fit coefficients of $R^2 = 0.969$ for the u-component and $R^2 = 0.902$ for the v-component, which can be regarded as a definite validation of the lidar measurements in the wind tunnel. The fact that both components are estimated that well, is a confirmation of the good synchronisation of the WindScanners.
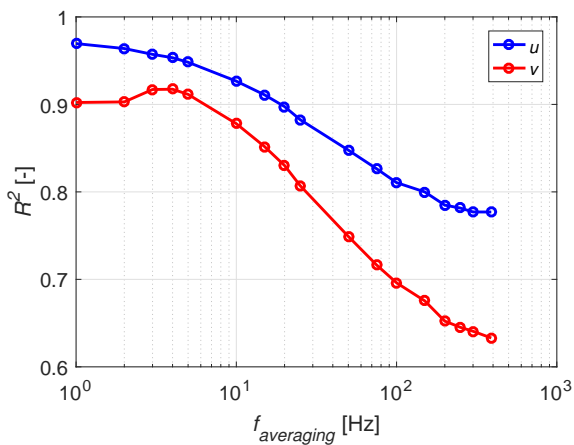
Figure 14. Goodness of fit parameter R^2 of the linear fit between the averaged u- and v-components of the lidar and the hot-wire as a function of averaging frequency.
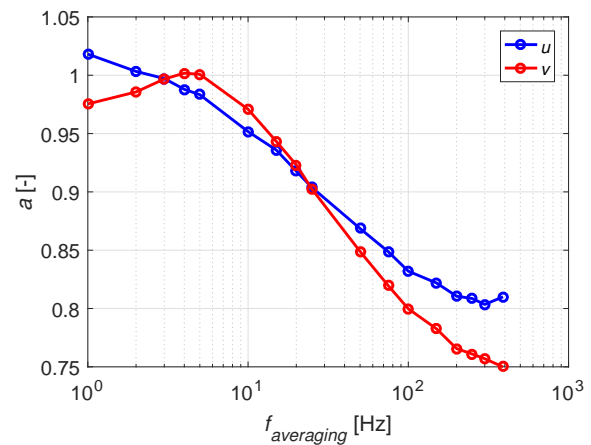
Figure 15. Slope a of the linear fit between the averaged u- and v-components of the lidar and the hot-wire as a function of averaging frequency.

Figures 14 and 15 show the influence of the averaging frequency on the goodness of fit R^2 and the regression line slope a of the linear fit, respectively. As expected, a better fit is yielded for lower averaging frequencies. In case of wake measurements,

it is important that the lidars are able to resolve the fluctuation scales induced by the wind turbines. Since the rated rotor speed is equal to 850 rpm, which is approximately 14 Hz, also the time series with this averaging rate were compared. The goodness of fit coefficients were $R^2 = 0.916$ for the u-component and $R^2 = 0.860$ for the v-component in this case.

To analyse the capability of measuring turbulence with lidars (Sathe and Mann, 2013), the spectrum of the u-component
5 of both the lidar and the hot-wire are plotted in Fig. 16. Since the sampling frequencies of the hot-wire probe and the lidars are 2500 Hz and 390 Hz, respectively, the boundary of the plot was chosen to be the Nyquist frequency based on the lidar, which equals 195 Hz. The lidar measurements are based on the backscatter of aerosols in a small measurement volume with a length of approximately 10 cm in this case and therefore turbulent structures with a size smaller than this measurement probe volume are partly filtered out. By applying Taylor's Theorem (Taylor, 1938) one can calculate that the lidars can resolve
10 temporal turbulence scales up to $\frac{1}{2} \cdot 5.6$ m s^{-1}/0.1 m = 28 Hz in this case. This line is marked in Fig. 16. It can be seen that the lidar indeed shows less power in the spectrum than the hot-wire for the upper frequency range. The drop in the slope of the spectrum does not exactly coincide with the 28 Hz frequency mark, because the intrinsic Lorentzian spatial weighting function of a continuous-wave lidar extends beyond the defined bounds of the probe length, therefore also acting as a filter on lower frequencies. The effect of spatial weighting is explained in detail by Sjöholm et al. (2009). Also combining measurements from
15 two lidars that each have a different probe volume (see Fig. 4), causes an even larger effect of averaging out small turbulence scales over a more complex volume.
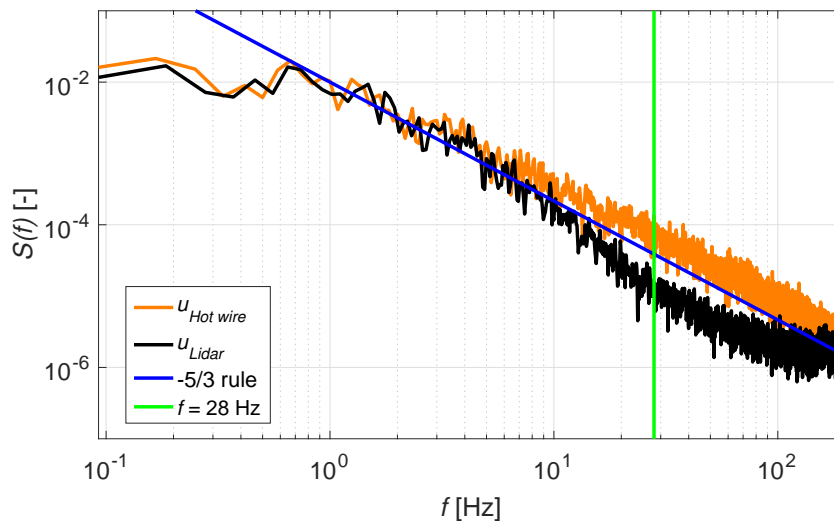
Figure 16. Turbulence spectrum of the u-component.

3.2 Measurement of wake profiles along a horizontal line

In Figs. 17 and 18, the respective u- and v-components of the wind speed evaluated from the line-of-sight measurements of both lidars of the transverse wake profile at hub height at a distance of $3D$ downstream of the first turbine can be seen. Both

components are normalised with respect to the free-stream velocity $u_0 = 5.67$ m s^{-1}. The data availability was 87.9%, due to the blockage effect of the wind turbine blades. All single measurements recorded with 390 Hz over a 1-minute period are plotted, as well as a bin averaged line with its standard deviation ($\pm 1\sigma$) bounds. The scatter of the measurements is reasonable and a smooth wake profile is produced. It is interesting to note that the v-component is almost zero on average, but it has a

5 highly turbulent behaviour at the wake boundaries. This could be caused by tip vortices as well as the high velocity gradient at the boundaries of the wake.
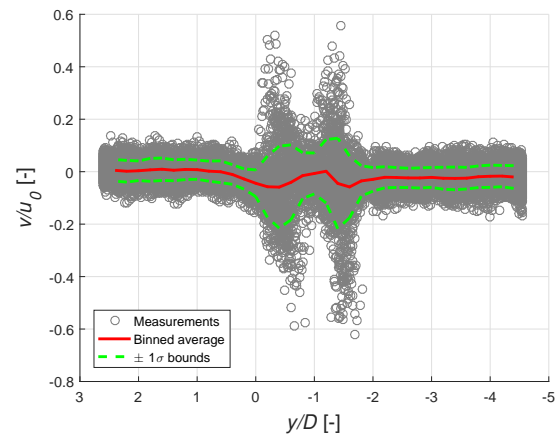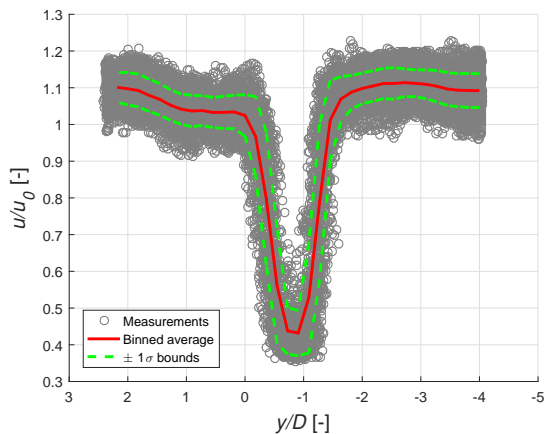
Figure 17. Wake profile expressed in the evaluated u-component, at $3D$ behind the first turbine with a $20°$ yaw angle.

Figure 18. Wake profile expressed in the evaluated v-component, at $3D$ behind the first turbine with a $20°$ yaw angle.

3.3 Measurement of horizontal wake area scans

The flexibility of the WindScanners allows for programming synchronised scan patterns that cover any desired plane or volume

10 in space. The scanning pattern sketched in Fig. 3 was used to map a horizontal plane at hub height containing the wake of all three wind turbines. Note that at the far end of the scan, the lidar units are measuring at a focus distance of about 20 m, which results in a probe length of about 50 cm locally. In Fig. 19 the normalised line-of-sight component measured by R2D3 is plotted, as the result of one scan iteration (upper) and as an average of 30 scan iterations (lower). This amount of iterations corresponds approximately to a 10-minute period. Although some blocking of the data is expected from the moving wind

15 turbine blades, still the measurement availability after filtering of 89.4% is satisfying. The normalised u- and v-components, calculated through Eq. (1), are plotted in Fig. 20. It illustrates that the lidars are successful in determining local 2D effects in wind turbine wake structures. The plot of the u-components shows a smooth and overlapping triple wake, enabled by the low turbulence in the wind tunnel. The non-zero local v-components are indicating the initial flow expansion in the induction zone of each of the turbines, as well as tip vortex effects on the wake boundary in the wakes. Interesting to note is that these effects

20 are well visible in the upper part of the plot, whereas in the lower part of the wake these effects are averaged out due to the larger turbulence in the region where the wakes from the three turbines partly overlap.
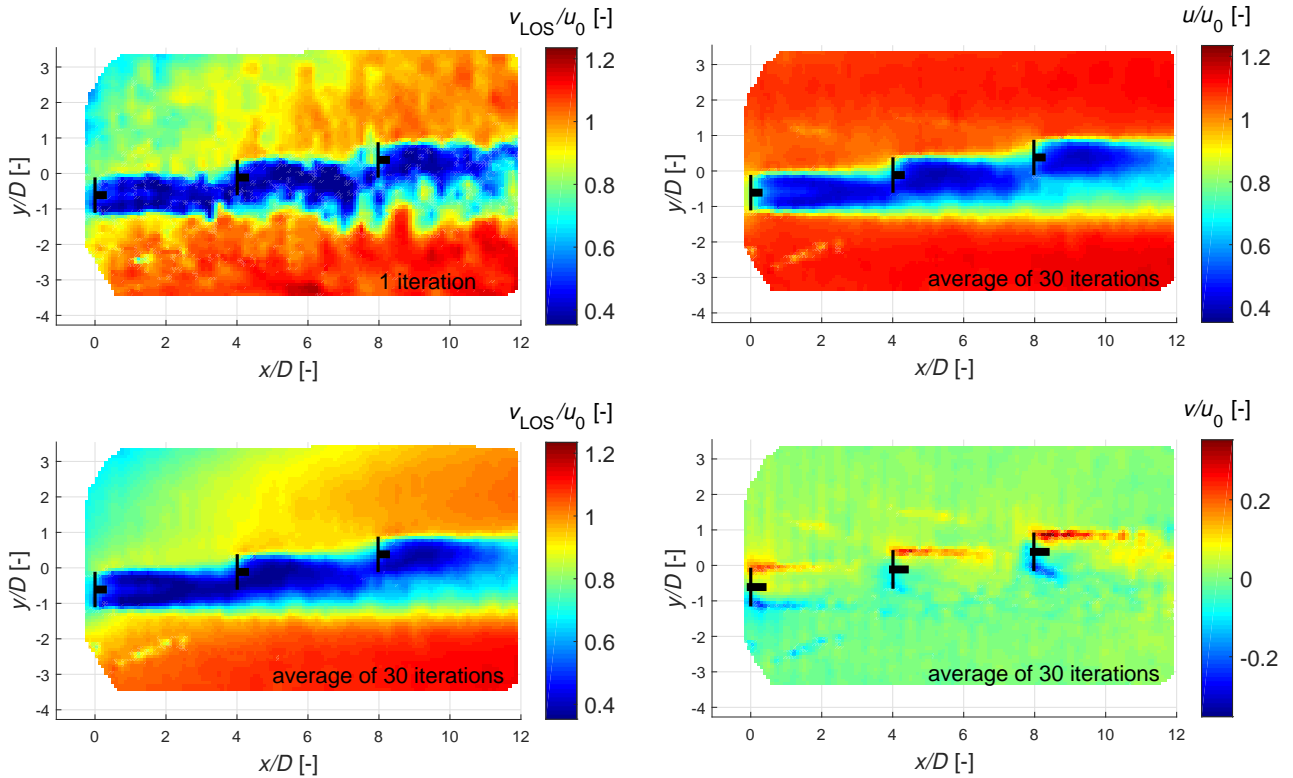
Figure 19. Wake wind field expressed in the line-of-sight component of R2D3.

Figure 20. Wake wind field expressed in the evaluated u- and v-components.

Note that it is hard to give any hard conclusions on the lidars' ability to measure small-scale turbulent fluctuations for this case, since the temporal resolution of the scans is not sufficient to track them. The wind field 'refreshing time' is in the order of a few seconds, whereas a single scan took 18.5 s to complete. This is a direct consequence of the small scale of the experiment and the trade-off that was made between spatial and temporal accuracy.

3.4 Uncertainty analysis

It is of particular interest how the dual-Doppler reconstruction affects the uncertainty of the estimated u- and v-components, according to a standard uncertainty propagation method (JCGM, 2008). Similar analyses have already been carried out by Stawiarski et al. (2013) and van Dooren et al. (2016b). The method described here considers both the lidar measurement uncertainty itself, as well as the artificially added uncertainty of the dual-Doppler reconstruction. The inputs are:

1. The uncertainty of each measured line-of-sight wind speed $e_{v_{LOS}}$, assumed to be 1% of the free-stream velocity

2. The pointing error for both the elevation and azimuth angles, e_δ and e_χ respectively, assumed to be 0.5 mrad ($\approx 0.03°$)

Solving the linear system in Eq. (1), one can express the quantities u and v individually:

$$u = \frac{\sin(\chi_2)\cos(\delta_2)v_{LOS_1} - \sin(\chi_1)\cos(\delta_1)v_{LOS_2}}{\cos(\delta_1)\cos(\delta_2)\sin(\chi_2 - \chi_1)} \qquad (3)$$

$$v = \frac{\cos(\chi_1)\cos(\delta_1)v_{LOS_2} - \cos(\chi_2)\cos(\delta_2)v_{LOS_1}}{\cos(\delta_1)\cos(\delta_2)\sin(\chi_2 - \chi_1)} \qquad (4)$$

The numerical errors e_u and e_v of the respective velocity components u and v are then expressed as follows:

$$5 \quad e_u = \sqrt{\left(\frac{\partial u}{\partial v_{LOS_1}}e_{v_{LOS_1}}\right)^2 + \left(\frac{\partial u}{\partial v_{LOS_2}}e_{v_{LOS_2}}\right)^2 + \left(\frac{\partial u}{\partial \chi_1}e_{\chi_1}\right)^2 + \left(\frac{\partial u}{\partial \chi_2}e_{\chi_2}\right)^2 + \left(\frac{\partial u}{\partial \delta_1}e_{\delta_1}\right)^2 + \left(\frac{\partial u}{\partial \delta_2}e_{\delta_2}\right)^2} \qquad (5)$$

$$e_v = \sqrt{\left(\frac{\partial v}{\partial v_{LOS_1}}e_{v_{LOS_1}}\right)^2 + \left(\frac{\partial v}{\partial v_{LOS_2}}e_{v_{LOS_2}}\right)^2 + \left(\frac{\partial v}{\partial \chi_1}e_{\chi_1}\right)^2 + \left(\frac{\partial v}{\partial \chi_2}e_{\chi_2}\right)^2 + \left(\frac{\partial v}{\partial \delta_1}e_{\delta_1}\right)^2 + \left(\frac{\partial v}{\partial \delta_2}e_{\delta_2}\right)^2} \qquad (6)$$

The first two terms of the square root, i.e. containing the partial derivatives with respect to the line-of-sight speed, formed the largest contribution to both e_u and e_v. The derivatives with respect to the scanning angles had less influence for the current

10   measurement setup.

To include the uncertainty introduced by measuring in the wind turbine wake region, which is characterised by large spatial gradients, the 10-minute averaged wind fields are used to estimate these gradients and execute a precision study on the effect of a small pointing error on the actual measurement. Especially at the far end of the measurement domain, a small angular offset of 0.03° could cause a dislocation of the measurement point in the y-direction of 1 cm. When measuring a small scale effect

15   such as a wake, this displacement could affect the uncertainty significantly. In the following, we only consider the uncertainty in the y-direction, assuming this has the most significant contribution. Namely, the gradients in this direction are much steeper than in the x-direction, with an exception for the near vicinity of the rotor plane.

The uncertainty e_y can be expressed in the azimuth angle pointing accuracy as follows:

$$e_y = \left(\sin\left(\chi + \frac{1}{2}e_\chi\right) - \sin\left(\chi - \frac{1}{2}e_\chi\right)\right)f \qquad (7)$$

20   With this information, we are able to include an error on the u-component of the velocity according to the gradients in y-direction by means of the following uncertainty estimate:

$$e_{u_{wake}} = \frac{\partial u}{\partial y}e_y \qquad (8)$$

The partial derivative $\frac{\partial u}{\partial y}$ is calculated numerically with a first order central finite difference coefficient based on the 10-minute averaged measurement itself (see the top graph in Fig. 20).
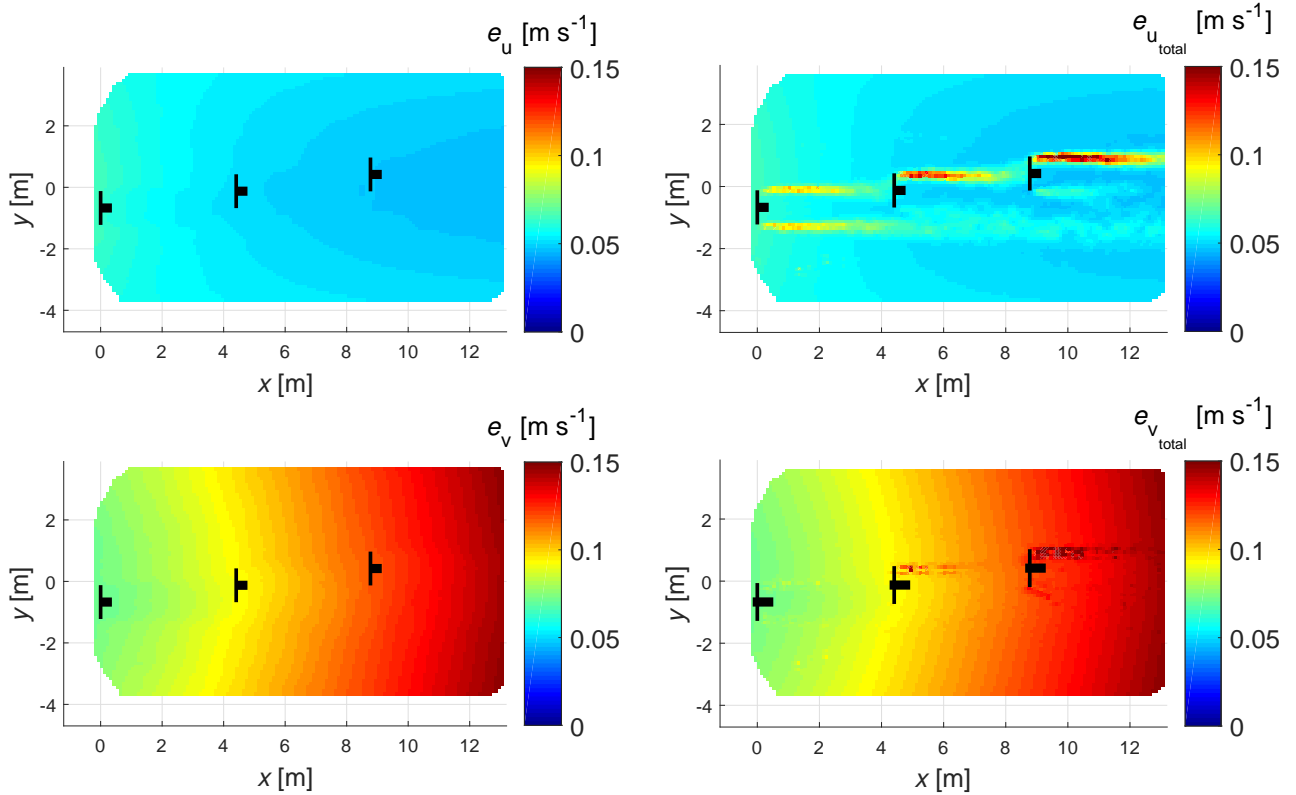
Figure 21. Dual-Doppler uncertainty on the evaluated u- and v-components.

Figure 22. Dual-Doppler uncertainty on the evaluated u- and v-components including wake gradient error.

Finally, the total uncertainty including the wake effect can be calculated as such:

$$e_{u_{total}} = \sqrt{e_u^2 + e_{u_{wake}}^2} \qquad (9)$$

In Fig. 21 the 10-minute averaged uncertainty plots of both the evaluated u- and v-components, e_u and e_v respectively, are

5   presented. It can be seen that the error e_v is larger than e_u overall. In the plot of e_u it can be seen that the error decreases slightly while moving from left to right. This is caused by the better alignment of the lidar beams with the x-direction. More interesting to analyse is the error on the v-component. It shows a significant increase towards the right of the measurement domain. This is related to the difference in azimuth angles between the two lidars, i.e. the lidar beams become more aligned with each other and thus have less potential to accurately resolve two orthogonal wind speed components. When the difference

10   between the azimuth angles $|\Delta\chi| = |\chi_1 - \chi_2|$ tends towards $180°$, the u-component cannot be resolved anymore and when $|\Delta\chi|$ tends towards $0°$, this applies to the v-component. To the far left of our measurement domain, $|\Delta\chi| \approx 90°$, which is the ideal case for dual-Doppler wind field reconstruction. To the far right of the plot, this angle difference decreases to $|\Delta\chi| \approx 30°$.

In Fig. 22 the respective total uncertainties $e_{u_{total}}$ are plotted, which include an error component related to the wake boundary gradients. As expected, an increased uncertainty around the boundaries is calculated, which gets larger with increasing distance from the lidars. Particularly interesting is that on the lower part of the plots, the overlapping wakes from the three wind turbines smooth out the gradients, thus let the error be smaller than at the upper and steeper wake boundaries.
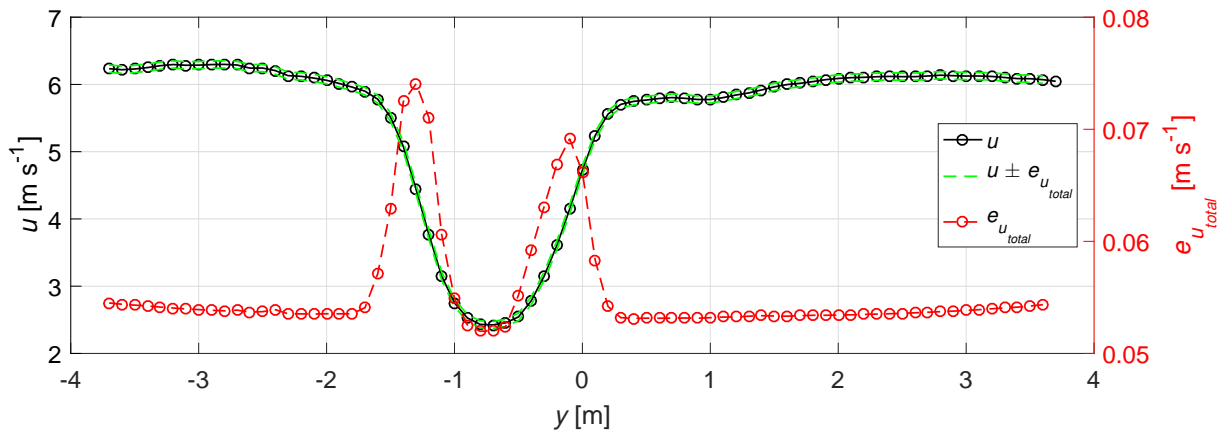
Figure 23. Average wake profile cross-section at a $2D$ downstream distance ($x = 2.2$ m) from the first turbine, with the total error indicated.

5   To get a better feeling for the magnitude of the additional error caused by the wake boundary gradients, Fig. 23 shows a wake profile at $2D$ downstream distance from turbine one, extracted from Fig. 22. Relative to the actual wake profile, the error bounds cannot be distinguished easily, but when observing the total error $e_{u_{total}}$ separately, an increase of up to 40% with respect to the error e_u can be noticed. This value will increase further when performing the same analysis further downstream. This confirms that one has to be careful with lidar measurements in wind fields containing large gradients, even if the systems

10   are known to have a high pointing accuracy.

4   Conclusions

A first measurement campaign with short-range synchronised lidar WindScanner measurements in a wind tunnel demonstrated that this technology can be used to measure both the wind tunnel mean flow and turbulence as well as wake profiles of scaled wind turbines. Validation was performed successfully by comparing the lidar measurements with commonly used hot-wire

15   probes. Because of the lidar measurement principle, between 10-15% of the data is lost due to the moving wind turbine blades in the measurement region. Additionally, the lidar systems cannot resolve the smallest turbulence scales due to the finite measurement probe volumes which are significantly larger than those of the hot-wire probes. Also an extensive uncertainty analysis showed that increased errors occur in regions with steep spatial velocity gradients. However, lidar as a remote sensing application has the significant benefit that it does not influence the flow by its presence, contrary to the hot-wire probes,

20   which have to be mounted on a beam structure that potentially disturbs the flow. Also, the WindScanner technology enables

scanning and mapping of entire two-dimensional horizontal and vertical wind fields within seconds to minutes. It is therefore our conclusion that scanning wind lidars have significant potential for future wind tunnel measurement applications.

Author contributions. M. F. van Dooren had the lead of both measurement analysis and paper writing. F. Campagnolo wrote the paragraph on the model wind turbines and provided further information about the measurement campaign. M. Sjöholm, N. Angelou and T. Mikkelsen

5   designed the lidar measurement scenarios, performed the lidar measurement campaign, post-processed the lidar data, provided assistance in the lidar data analysis and interpretation, wrote parts of the content on the lidars, and critically reviewed the paper multiple times. M. Kühn initiated the measurement campaign, provided ideas for the scientific scope of the paper and had a supervising role.

Competing interests. The authors declare that they have no conflict of interest.

Acknowledgements. This work is partly funded by the German Ministry of Economic Affairs and Energy in the scope of the CompactWind

10 project (Ref. Nr. 0325492B/D). Special thanks go out to all authors involved with the original work for the TORQUE 2016 conference: V. Petrović from the University of Oldenburg, C. L. Bottasso from the Technical University of Munich, and A. Croce and A. Zasso from the Politecnico di Milano. The authors also wish to thank all engineers and technicians who made this work possible: L. Ronchi, G. Campanardi, S. Giappino and D. Grassi from the Politecnico di Milano and P. Hansen and C. B. M. Pedersen from DTU Wind Energy.

References

Bottasso, C. L., Campagnolo, F., and Petrović, V.: Wind Tunnel Testing of Scaled Wind Turbine Models: Beyond Aerodynamics, Journal of Wind Engineering and Industrial Aerodynamics, 127, 11–28, doi:10.1016/j.jweia.2014.01.009, 2014.

Campagnolo, F., Petrović, V., Schreiber, J., Nanos, E. M., Croce, A., and Bottasso, C. L.: Wind Tunnel Testing of a Closed-Loop Wake Deflection Controller for Wind Farm Power Maximization, Journal of Physics: Conference Series, 753, doi:10.1088/1742-6596/753/3/032006, 2016.

JCGM: Evaluation of Measurement Data: Guide to the Expression of Uncertainty in Measurement, Tech. rep., Joint Committee for Guides in Meteorology, JCGM 201X CD, 2008.

Mikkelsen, T.: About WindScanner.eu, Official Webpage, http://www.windscanner.eu/About-WindScanner, Accessed: 1/6/2016, 2012.

Rockel, S., Camp, E., Schmidt, J., Peinke, J., Cal, R. B., and Hölling, M.: Experimental Study on Influence of Pitch Motion on the Wake of a Floating Wind Turbine Model, Energies, 7, 1954–1985, doi:10.3390/en7041954, 2014.

Sathe, A. and Mann, J.: A Review of Turbulence Measurements Using Ground-Based Wind Lidars, Atmos. Meas. Tech., 6, 3147–3167, doi:10.5194/amt-6-3147-2013, 2013.

Simley, E., Angelou, N., Mikkelsen, T., Sjöholm, M., Mann, J., and Pao, L. Y.: Characterization of Wind Velocities in the Upstream Induction Zone of a Wind Turbine Using Scanning Continuous-Wave Lidars, Journal of Renewable and Sustainable Energy, 8, doi:10.1063/1.4940025, 2016.

Sjöholm, M., Mikkelsen, T., Mann, J., Enevoldsen, K., and Courtney, M.: Spatial Averaging Effects of Turbulence Measured by a Continuous-Wave Coherent Lidar, Meteorologische Zeitschrift, 18, doi:10.1127/0941-2948/2009/0379, 2009.

Stawiarski, C., Träumner, K., Knigge, C., and Calhoun, R.: Scopes and Challenges of Dual-Doppler Lidar Wind Measurements - An Error Analysis, J. Atmos. Oceanic Technol., 30, 2044–2064, doi:10.1175/JTECH-D-12-00244.1, 2013.

Taylor, G. I.: The Spectrum of Turbulence, Proc. Roy. Soc. London, 164, 476–490, 1938.

van Dooren, M. F., M. Kühn, V. P., Bottasso, C. L., Campagnolo, F., Sjöholm, M., Angelou, N., Mikkelsen, T., Croce, A., and Zasso, A.: Demonstration of Synchronised Scanning Lidar Measurements of 2D Velocity Fields in a Boundary-Layer Wind Tunnel, Journal of Physics: Conference Series, 753, doi:10.1088/1742-6596/753/7/072032, 2016a.

van Dooren, M. F., Trabucchi, D., and Kühn, M.: A Methodology for the Reconstruction of 2D Horizontal Wind Fields of Wind Turbine Wakes Based on Dual-Doppler Lidar Measurements, Remote Sensing, 8, doi:10.3390/rs8100809, 2016b.

Wagner, R., Vignaroli, A., Angelou, N., Sathe, A., Forsting, A. R. M., M, Sjöholm, and Mikkelsen, T.: Measurement of Turbine Inflow with a 3D WindScanner System and a SpinnerLidar, in: DEWEK 2015, Bremen, 2015.

Zasso, A., Giappino, S., Muggiasca, S., and Rosa, L.: Optimization of the Boundary Layer Characteristics Simulated at Politecnico di Milano Boundary Layer Wind Tunnel in a Wide Scale Ratio Ranges, Tech. rep., Dipartimento di Meccanica - Politecnico di Milano, 2005.